Article

Fluoroscopic 3D Image Generation from Patient-Specific PCA Motion Models Derived from 4D-CBCT Patient Datasets: A Feasibility Study

Salam Dhou[1,*], Mohanad Alkhodari[2], Dan Ionascu[3], Christopher Williams[4] and John H. Lewis[5]

[1] American University of Sharjah, Sharjah, United Arab Emirates; sdhou@aus.edu
[2] Khalifa University, Abu Dhabi, United Arab Emirates; mohanad.alkhodari@ku.ac.ae
[3] University of Cincinnati, Cincinnati, OH 45267, United States of America; ionasctn@ucmail.uc.edu
[4] Brigham and Women's Hospital and Harvard Medical School, Boston, MA 02115, United States of America; cwilliams@bwh.harvard.edu
[5] Cedars-Sinai Medical Center, Los Angeles, CA 90048, United States of America; john.h.lewis@cshs.org
* Correspondence: sdhou@aus.edu; Tel.: +97165152943

Abstract: A method for generating fluoroscopic (time-varying) volumetric images using patient-specific motion models derived from 4-dimensional cone-beam CT (4D-CBCT) images is developed. 4D-CBCT images acquired immediately prior to treatment have the potential to accurately represent patient anatomy and respiration during treatment. Fluoroscopic 3D image estimation is done in two steps: 1) deriving motion models and 2) optimization. To derive motion models, every phase in a 4D-CBCT set is registered to a reference phase chosen from the same set using deformable image registration (DIR). Principal components analysis (PCA) is used to reduce the dimensionality of the displacement vector fields (DVFs) resulting from DIR into a few vectors representing organ motion found in the DVFs. The PCA motion models are optimized iteratively by comparing a cone-beam CT (CBCT) projection to a simulated projection computed from both the motion model and a reference 4D-CBCT phase, resulting in a sequence of fluoroscopic 3D images. Patient datasets were used to evaluate the method by estimating the tumor location in the generated images compared to manually defined ground truth positions. Experimental results showed that the average tumor mean absolute error (MAE) along the superior-inferior (SI) direction and the 95th percentile in two patient datasets were (2.29 mm and 5.79 mm) for patient 1 and (1.89 mm and 4.82 mm) for patient 2. This study has demonstrated the feasibility of deriving 4D-CBCT-based PCA motion models that have the potential to account for the 3D non-rigid patient motion and localize tumors and other patient anatomical structures on the day of treatment.

Keywords: principal component analysis (PCA); motion model; respiratory-correlated four-dimensional cone-beam CT (4D-CBCT); lung cancer; stereotactic body radiotherapy (SBRT), image-guided radiation therapy (IGRT)

1. Introduction

Respiratory-induced organ motion is a major source of uncertainty in stereotactic body radiotherapy (SBRT) of thoracic and upper abdominal cancers [1]. Respiratory motion can result in motion artifacts during image acquisition and limitations in both radiotherapy planning and delivery. Respiratory-correlated, or four-dimensional (4D) computed tomography (4DCT), as an image-guided radiation therapy (IGRT) tool, provides a solution to obtain high quality CT images in the presence of respiratory motion [2]. Thus, 4DCT became a standard method in radiotherapy treatment planning to account for organ motion, reduce motion artifacts, and reduce associated uncertainties.

Image-based motion modeling of patient anatomy during radiotherapy can be useful in accurately localizing tumors and other anatomical structures in the body [3–7]. There are many approaches proposed for image-based motion modeling. Principal component

analysis (PCA)-based motion modeling has proven its efficacy in representing the spatio-temporal relationship of the entire lung motion [8]. Because of their compactness and performance, PCA motion models are being used along with projection images captured at the day of treatment for generating time-varying volumetric images, often called fluoroscopic because they are produced in a continuous fashion similar to the images produced using the well-known fluoroscopy procedure [9–16]. PCA motion models are derived by applying PCA on the displacement vector fields (DVFs) that result from applying deformable image registration (DIR) between the 4DCT phases and a reference phase chosen from the same set. PCA distills the large dataset of DVFs into a few eigenvectors and coefficients representing lung motion [8,12,14,16,17]. Since 4DCT images are acquired at the time of treatment planning, which happens days or weeks before the treatment delivery day, PCA motion models derived from them may not accurately represent patient anatomy or motion patterns at the day of treatment delivery [14]. Consequently, they may not account for tumor baseline shifts that are observed frequently in the clinic [18].

Respiratory-correlated, or four-dimensional (4D) cone-beam CT (4D-CBCT) has been introduced and used in radiotherapy for many clinical tasks such as image guidance and target verification just prior to treatment delivery [19]. 4D-CBCTs are reconstructed by first assigning the raw CBCT projections into several bins depending on the respiratory phases they exhibit, then, 3D images are reconstructed from each bin. Several methods have been used to estimate respiratory motion corresponding to the raw CBCT projections. These methods include using external equipment, such as external markers or abdominal belts, internal implanted radiopaque fiducial markers, or marker-free pure image-based approaches [20–27]. On-board 4D-CBCT images are produced at the day of treatment delivery while the patient is in treatment position. Thus, motion models derived from 4D-CBCT images have the potential to account for the inter-fraction anatomical motion variations that can occur between the planning and treatment delivery phases, which may not be handled using 4DCT-based motion models.

Previous research has been conducted to derive PCA motion models from 4D-CBCT images [9,10,28,29]. In [9,10], PCA motion models were derived from datasets of 4D-CBCT images of simulated patients using the XCAT phantom [30–32] and an anthropomorphic physical phantom. This work showed the feasibility and reliability of estimating anatomical motion using 4D-CBCT-based motion models compared to 4DCT-based motion models. However, the experiments were only applied to phantom datasets and hence its efficacy on clinical patient datasets has not been verified. In another study, PCA motion models were derived from datasets of patients' 4D-CBCT images taken at different treatment days to quantify the inter-fraction variations of these motion models [28,29]. However, these 4D-CBCT-based PCA motion models were not applied for further clinical tasks such as generating fluoroscopic 3D images or localizing tumors and/or other anatomical structures of the patients at the time of treatment delivery.

In this paper, we propose to: 1) derive PCA motion models from patient 4D-CBCT images captured immediately before treatment delivery; and 2) use these 4D-CBCT-based motion models to estimate fluoroscopic 3D images based on CBCT projections captured immediately before treatment delivery. The proposed work is an extension to the previous work [9,10] where the methods were tested on digital phantom datasets and anthropomorphic physical phantom datasets. In this paper, the methods are applied on patient datasets to demonstrate the feasibility of considering this approach in clinical settings. The rest of the paper is organized as follows. Section 2 presents the materials and methods. Section 3 presents the experimental results. The results are discussed in Section 4. Section 5 concludes the paper.

2. Materials and Methods

2.1. Datasets

Preprints (www.preprints.org) | NOT PEER-REVIEWED | Posted: 29 November 2021 doi:10.20944/preprints202111.0519.v1

CBCT projections for two patients were acquired using the Elekta Synergy system (Elekta Oncology Systems Ltd., Crawley, West Sussex, UK) and used retrospectively in this study. This retrospective research protocol qualified for exempt approval from the Institutional Review Board (IRB) of the American University of Sharjah, United Arab Emirates, on August 23, 2021 (IRB 18-425). The projections were acquired over 200 degree rotations at 5.5 fps in 4 minutes. The total number of projections is 1320 in the first patient dataset and 1356 in the second patient dataset. The dimensions of the projections are 512 × 512 pixels in both datasets. 4D-CBCT images were reconstructed from each projection dataset. To do so, the projections were sorted into six phase bins according to their corresponding respiratory status estimated using the "Amsterdam Shroud" method [33,34]. The FDK reconstruction algorithm [35] implemented in Reconstruction ToolKit (RTK) [36] was used to reconstruct 3D images from each projection bin which resulted in 4D-CBCT images of six phases. The dimensions of each of the reconstructed images are 176 × 228 × 256 voxels, with 1.1 as the voxel size.

The ground truth tumor location for the patient datasets was found by manually identifying the diaphragm location in each projection. A simple graphical user interface was programmed in MATLAB (The MathWorks, Inc., Natick, Massachusetts, USA) and used for that purpose. To estimate the coordinates of the tumor in each projection, the diaphragm apex coordinates were identified in each projection and used in a linear regression model to estimate the tumor coordinates. To compare the ground truth 2D coordinates with the tumor 3D coordinates in the estimated fluoroscopic 3D images, the tumor coordinates in the estimated fluoroscopic 3D images are projected onto a 2D flat panel detector. The distance between the 2D projected and ground truth coordinates was calculated in the plane of the detector, and then scaled down to an approximate error inside the patient (at isocenter). A similar procedure was followed in previous publications [10,16,37].

Figure 1 shows axial, coronal, and sagittal slices of peak-exhale 4D-CBCT from each patient. The peak-exhale phase phase was selected as the reference phase to which all other 4D-CBCT phases are deformed in the DIR module.

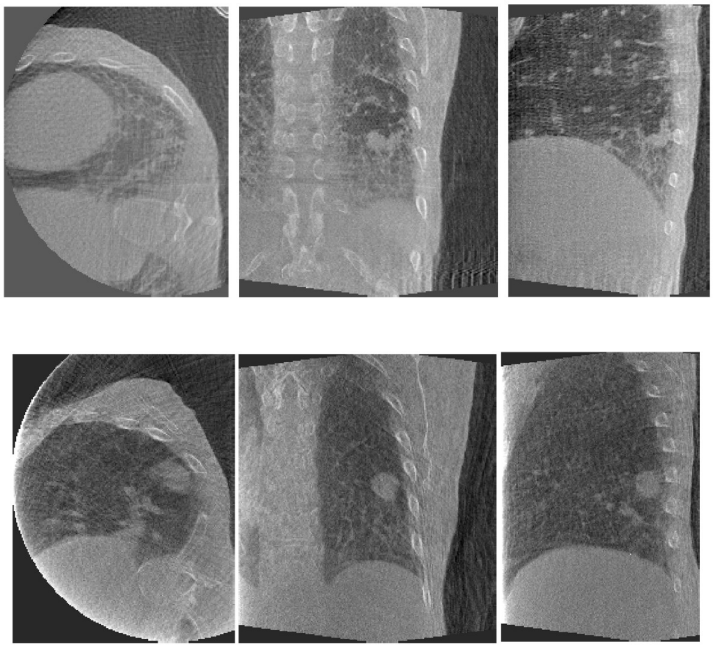

(a) (b) (c)

Figure 1. Sample phase (peak-exhale) 4D-CBCT from patient #1 (top) and patient #2 (bottom): (a) axial, (b) coronal, (c) sagittal slices.

Preprints (www.preprints.org) | NOT PEER-REVIEWED | Posted: 29 November 2021 doi:10.20944/preprints202111.0519.v1

2.2. Fluoroscopic 3D image estimation

Fluoroscopic 3D image estimation is accomplished in two steps:

2.2.1. 4D-CBCT-based motion model estimation

DIR is applied to each 4D-CBCT phase with respect to a reference phase chosen from the same set. In this work, the peak-exhale phase was chosen as the reference phase. A Demons DIR algorithm implemented on a graphics processing unit (GPU) is used in this study [38]. Applying DIR on pairs of phases results in a set of DVFs describing the voxel-wise displacements between each pair of phases.

As the resulting DVFs represent a huge dataset, a dimensionality reduction approach is used to transform this dataset from the original high-dimensional space into a low-dimensional one while retaining the properties of the original data. PCA was employed as a linear dimensionality reduction method. PCA is applied on the DVFs which results in a set of eigenvectors and eigenvalues representing the motion of the patient [8]. The set of DVFs can be represented as a weighted sum of these eigenvectors and eigenvalues as follows:

$$\boldsymbol{D} = \bar{\boldsymbol{D}} + \sum_{i=1}^{N} \boldsymbol{v_i}\, \boldsymbol{u_i}(\boldsymbol{t}), \qquad (1)$$

where $\boldsymbol{D}$ is the DVF dataset, $\bar{\boldsymbol{D}}$ is the mean DVF, $\boldsymbol{u_i}(\boldsymbol{t})$ are the PCA eigenvalues defined in time, $\boldsymbol{v_i}$ are the eigenvectors defined in space, and N is the number of eigenmodes considered. The eigenvectors can be sorted according to their corresponding eigenvalues such that eigenvectors corresponding to the largest eigenvalues represent large fraction of the variance of the original data. Previous studies have shown that the first few (2-3) eigenvectors, corresponding to the largest eigenvalues, are sufficient to represent the motion patterns existing in the original dataset [10,12,29]. In this work, the first three eigenvectors are considered as the motion model.

2.2.2 Optimization

An optimization approach is used to estimate the fluoroscopic 3D images. This approach involves three inputs: 1) the motion model (a set of 3 eigenvectors with corresponding eigenvalues); 2) the 4D-CBCT reference phase; and 3) the CBCT projections captured immediately before treatment, while the patient is in treatment position immediately before treatment. The working principle of this optimization approach is to iteratively update the motion model by minimizing a cost function representing the squared L_2-norm of the difference between a CBCT projection captured at treatment time and a 2D projection computed using both the motion model and the 4D-CBCT reference phase. The cost function is represented by:

$$\min_{\boldsymbol{u}} \boldsymbol{J}(\boldsymbol{u}) = \|\boldsymbol{P} \cdot \boldsymbol{f}(\boldsymbol{D}(\boldsymbol{u}), \boldsymbol{f_0}) - \boldsymbol{\lambda} \cdot \boldsymbol{x}\|, \qquad (2)$$

where $\boldsymbol{f_0}$ is the 4D-CBCT reference phase, $\boldsymbol{D}(\boldsymbol{u})$ are the parameterized DVFs, $\boldsymbol{f}$ is the estimated fluoroscopic 3D image, $\boldsymbol{P}$ is the projection matrix used to compute the projection from the fluoroscopic 3D image f, $\boldsymbol{x}$ is the CBCT projection at treatment delivery day, and $\boldsymbol{\lambda}$ is the relative pixel intensity between the 2D computed projection and the CBCT projection $\boldsymbol{x}$. The cost function is minimized using a version of gradient descent as explained in the appendix in [16]. Figure 2 presents the flowchart of the fluoroscopic 3D image estimation algorithm.

Preprints (www.preprints.org) | NOT PEER-REVIEWED | Posted: 29 November 2021 doi:10.20944/preprints202111.0519.v1

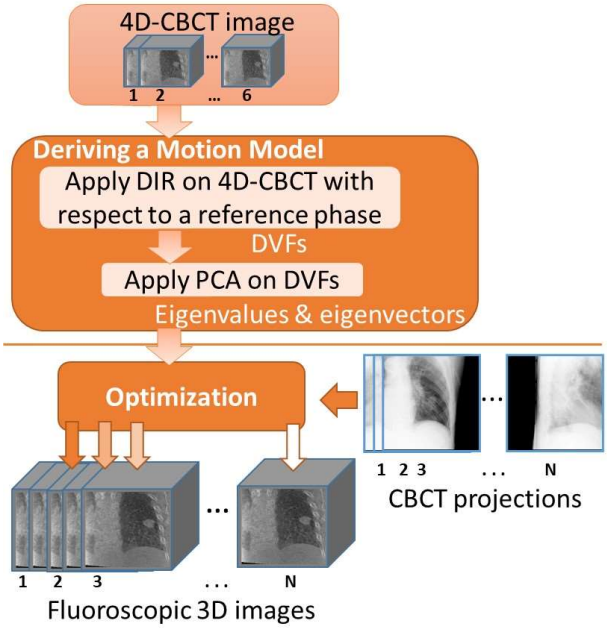

Figure 2. Flowchart of the fluoroscopic 3D image estimation algorithm

In this approach, a linear relationship between the intensities of the CBCT projections and the computed projections using the motion model is assumed. However, some factors may disturb this assumption such as noise and the quality of the 4D-CBCT images being used to compute the 2D projections. To reduce the effect of these factors, a region of interest (ROI) was chosen from both the CBCT projection and the computed projection to reduce the effect of the noise and artifacts existing in the whole images and enhance the accuracy of the optimization. The ROI was chosen to surround the tumor and the diaphragm which are the most visible structures in the image exhibiting breathing motion.

2.3. Evaluation

The method is evaluated by finding the tumor localization error, which is calculated as the mean absolute error (MAE) of the tumor centroid location in the estimated fluoroscopic 3D images. This error value is measured by taking the mean absolute difference between the tumor centroid location in the estimated fluoroscopic 3D images and the ground truth locations. The process of estimating ground truth tumor coordinates is described in 2.1. The 3D tumor coordinates in the estimated fluoroscopic 3D images are projected onto a 2D flat panel detector to be able to compare them with the 2D ground truth tumor coordinates. The error is measured along the superior-inferior (SI) direction in patient coordinates.

3. Results

In this section, the estimated motion models and fluoroscopic 3D images are evaluated. Figure 3 (a) shows the eigenvalue spectrum for the PCA motion models for patient #1 and patient #2. It can be observed that the eigenvalues decrease with higher eigenmodes and drop drastically after the third eigenmode in both patients. Figure 3 (b) shows the percentage of the variance explained by each eigenmode in each patient. It shows both the individual and cumulative explained variances. As can be seen from the figure, the first three eigenmodes can explain most of the variance (97.1% in patient #1) and (97.4% in patient #2).

Preprints (www.preprints.org) | NOT PEER-REVIEWED | Posted: 29 November 2021 doi:10.20944/preprints202111.0519.v1

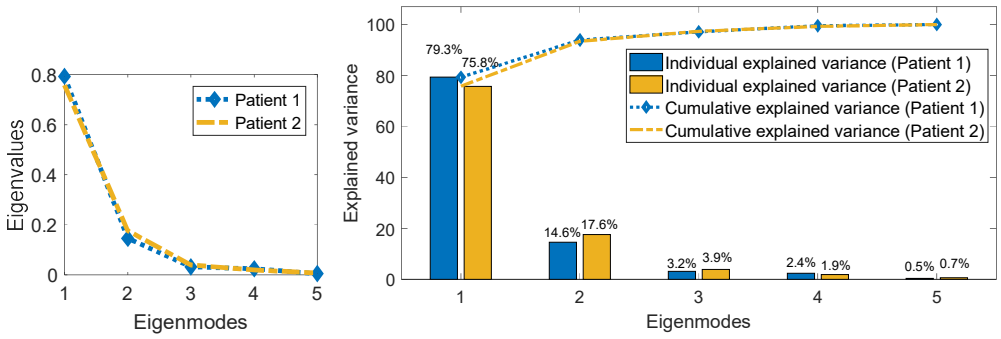

(a) (b)

Figure 3: Variance explained by eigenvectors. (a) eigenvalues' spectrum of the motion models of patient #1 and patient #2 (b) Explained variance ratio of the motion models of patient #1 and patient #2.

The PCA motion models derived from 4D-CBCT images were used to estimate the fluoroscopic 3D images. Figure 4 shows a CBCT projection and the corresponding 2D projection computed using the estimated motion model and the 4D-CBCT reference image. A scatter plot showing the linear correlation between the intensities of the two images is shown. As can be seen from the figure, a linear correlation is found with a correlation coefficient of 96%.

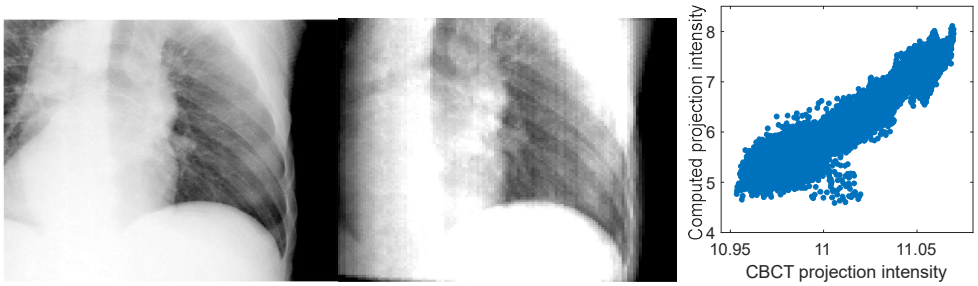

(a) (b) (c)

Figure 4. (a) sample CBCT projection from patient #2, (b) corresponding computed projection using the motion model and the 4D-CBCT reference phase, and (c) a scatter plot showing the correlation between the intensities of the two images in (a) and (b). A linear correlation is found between the two image intensities with a correlation coefficient of 96%.

Figure 5 shows axial, coronal, and sagittal slices of a sample estimated fluoroscopic 3D image from patient #2. Figure 6 shows coronal slices of two estimated fluoroscopic 3D images from patient #2 at different breathing phases. As can be noticed from Figure 6, the estimated fluoroscopic images were able to capture the anatomical motion represented in the CBCT projections used in the optimization module.

Preprints (www.preprints.org) | NOT PEER-REVIEWED | Posted: 29 November 2021 doi:10.20944/preprints202111.0519.v1

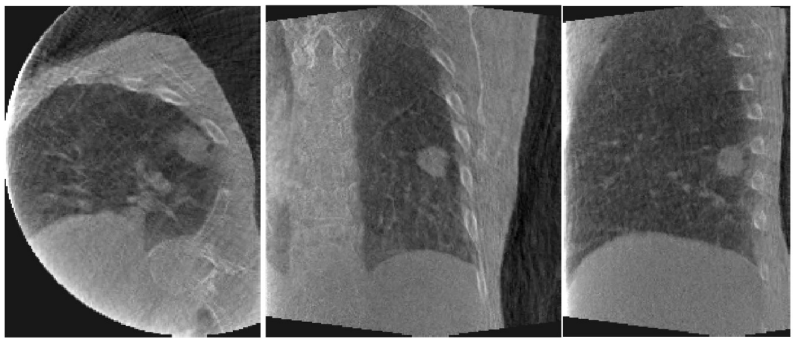

(a) (b) (c)

Figure 5. Sample estimated fluoroscopic 3D image from patient #2 dataset: (a) axial, (b) coronal, and (c) sagittal slices.

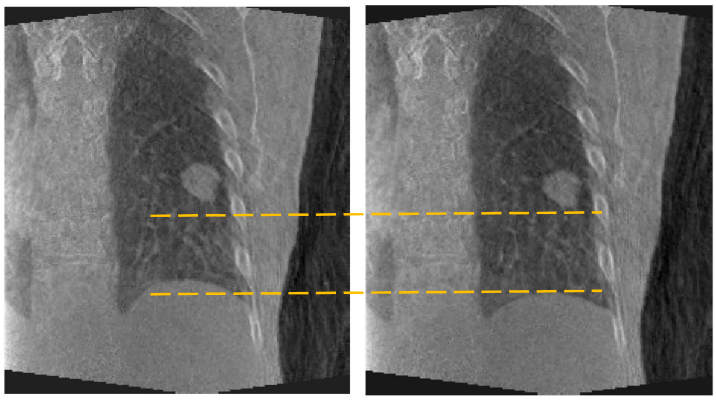

(a) (b)

Figure 6. Coronal slices of two estimated fluoroscopic 3D images from patient #2 dataset at different breathing phases.

To evaluate the accuracy of the estimated fluoroscopic images, the SI tumor position in the estimated images is estimated and compared to its ground truth location. Figure 7 shows the SI tumor position in all the estimated fluoroscopic 3D images compared to the ground truth tumor positions in mm for patient #1 (a) and patient #2 (b). The tumor MAE along the SI direction was 2.29 mm with 95th percentile of 5.79 mm for patient #1 and 1.89 mm with 95th percentile of 4.82 mm for patient #2.

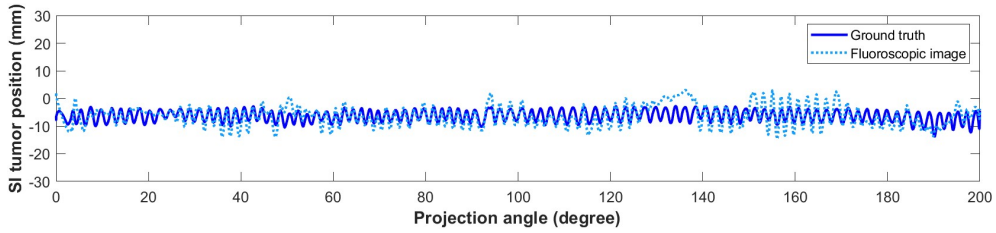

(a)

Preprints (www.preprints.org) | NOT PEER-REVIEWED | Posted: 29 November 2021 doi:10.20944/preprints202111.0519.v1

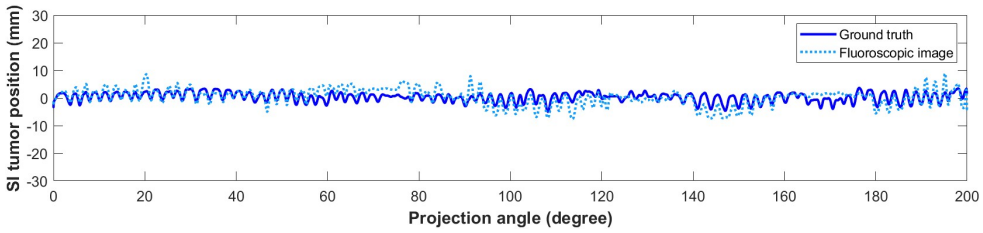

(b)

Figure 7. SI tumor position in the estimated fluoroscopic 3D images using motion models derived from 4D-CBCT images of patient #1 (a) and patient #2 (b).

4. Discussion

In this work, the feasibility of building patient-specific motion models from 4D-CBCT images and using them, along with a set of CBCT projections captured at the time of treatment delivery, to generate fluoroscopic 3D images has been studied. The 4D-CBCT-based motion models have the potential to overcome an important shortcoming of the 4DCT-based motion models in that they can reflect the patient anatomy and motion at the time of treatment delivery. These fluoroscopic 3D images can be used in several clinical applications such as delivered dose verification [39,40].

The methodology used in this work involved two main steps: deriving the PCA motion model and the optimization approach to estimate the fluoroscopic 3D images. The method was evaluated on two patient datasets. The resulting PCA 4D-CBCT-based motion models that were used in this work were analyzed in Section 3. As mentioned in Figure 3, the first few eigenmodes of these PCA motion models explained most of the variance in the DVF dataset. Based on this, the rest of the eigenmodes were dropped safely as they do not hold significant information. These results support the findings of other studies that have shown that a few eigenmodes (2-3) are sufficient to represent the organ motion represented by the DVFs [10,12,16,29]. The iterative optimization approach was shown to converge after several iterations which resulted in producing optimized fluoroscopic 3D images representing the anatomical motion of the patient. The algorithm was implemented to run efficiently on a GPU (NVIDIA GeForce GTX 1070, 8 GB VRAM). The DIR algorithm takes an average of 17.25 s to register a 4D-CBCT phase to the reference phase. The optimization step needs an average of 1.25 s to estimate a fluoroscopic 3D image, including the time required to estimate the tumor location.

Comparing this error to other studies using 4D-CBCT-based motion model derived from phantom datasets [10], it can be noticed that the error in this study is slightly higher. Given the complexities of the breathing patterns of the real patients and the poor quality of the 4D-CBCT images, having a higher tumor is expected. DIR accuracy is a key determinant of motion model accuracy. DIR yields the DVFs upon which the motion model is based. The DIR algorithm used in this study is the Demons algorithm [38]. In a previous fluoroscopic 3D image generation study using 4DCT images, the authors investigated the effect of DIR performance on the overall method accuracy [16]. It was observed that the error caused by DIR is negligible. In that study, the error was mainly attributed to optimization step of the method, specifically the mapping between the CBCT projection and the computed one.

One of the major challenges facing building motion models from 4D-CBCT images is the poor quality of the 4D-CBCT images used as input. The limited number of projections available for reconstruction of each 4D-CBCT bin are a key reason for the relatively poor quality of 4D-CBCT images. The effect of the quality of the 4D-CBCT images in fluoroscopic 3D image estimation has been investigated in [10]. The authors conducted an experiment using two sets of 4D-CBCT images simulated using digital XCAT phantom. The 4D-CBCT images in the first set were reconstructed from a well-sampled set of projections,

while the images in the second set were reconstructed from a severely under-sampled set of projections. The study showed that the tumor MAE along the SI direction has increased by 214% (from 1.28 mm to 4.02 mm) with a 95th percentile increasing by 250% (from 2.0 mm to 7.00 mm) when using the 4D-CBCT images that were reconstructed from an under-sampled set of projections as the input to this method. The normalized root mean square error (NRMSE) calculated using the voxel-wise intensity difference between the resulting estimated images and the ground truth images has also increased by 150% (from 0.10 mm to 0.25 mm) when using the 4D-CBCT images that were reconstructed from an under-sampled set of projections. The under-sampling issue in 4D-CBCT has been studied extensively in the literature. Several solutions to improve the quality of the 4D-CBCT images have been suggested, such as compressed sensing [41–45], motion compensated reconstruction [46–54], and interpolation of "in-between" projections to increase the number of projections in each respiratory phase bin [55–58]. Recently, deep learning approaches have been also proposed [59–61]. Motion modeling and fluoroscopic image estimation from enhanced 4D-CBCT images is worth investigating in future research.

5. Conclusions

This study investigated the feasibility of deriving motion models from patient 4D-CBCT images and using them to generate fluoroscopic 3D images of the patient on the treatment delivery day while the patient is in the treatment position. The algorithm consists of two steps. In the first step, PCA motion models were derived by performing PCA on the DVFs resulting from applying DIR on the input 4D-CBCT images. In the second step, an iterative optimization approach was applied on the motion model to generate a sequence of 3D images using CBCT projections. The estimated fluoroscopic 3D images were assessed by localizing the tumor in generated images and comparing these locations to the tumor ground truth location in the CBCT projections. The tumor MAE along the SI direction was 2.29 mm with 95th percentile of 5.79 mm for patient #1 and 1.89 mm with 95th percentile of 4.82 mm for patient #2. The clinical applications of this work include image guidance, patient positioning, and delivered dose estimation and/or verification.

Author Contributions: Conceptualization, Christopher Williams and John H. Lewis; Data curation, Salam Dhou, Mohanad Alkhodari and Dan Ionascu; Formal analysis, Salam Dhou, Dan Ionascu, Christopher Williams and John H. Lewis; Funding acquisition, Salam Dhou; Investigation, Salam Dhou; Methodology, Salam Dhou, Christopher Williams and John H. Lewis; Project administration, Salam Dhou; Resources, Salam Dhou and Dan Ionascu; Software, Mohanad Alkhodari; Supervision, John H. Lewis; Validation, Salam Dhou, Mohanad Alkhodari, Dan Ionascu, Christopher Williams and John H. Lewis; Visualization, Mohanad Alkhodari; Writing – original draft, Salam Dhou; Writing – review & editing, Mohanad Alkhodari, Dan Ionascu, Christopher Williams and John H. Lewis.

Funding: This research was funded by the American University of Sharjah, United Arab Emirates, grant number EFRG18-BBR-CEN-04. The content is solely the responsibility of the authors and does not necessarily represent the official views of the American University of Sharjah.

Institutional Review Board Statement: This retrospective research protocol qualified for exempt approval from the Institutional Review Board (IRB) of the American University of Sharjah, United Arab Emirates, on August 23, 2021 (IRB 18-425).

Conflicts of Interest: The authors declare no conflict of interest. The funders had no role in the design of the study; in the collection, analyses, or interpretation of data; in the writing of the manuscript, or in the decision to publish the results.

References

1. Keall, P.J.; Mageras, G.S.; Balter, J.M.; Emery, R.S.; Forster, K.M.; Jiang, S.B.; Kapatoes, J.M.; Low, D.A.; Murphy, M.J.; Murray, B.R.; et al. The management of respiratory motion in radiation oncology report of AAPM Task Group 76. *Med Phys* **2006**, *33*, 3874–3900.
2. Vedam, S.S.; Keall, P.J.; Kini, V.R.; Mostafavi, H.; Shukla, H.P.; Mohan, R. Acquiring a four-dimensional computed

tomography dataset using an external respiratory signal. *Phys Med Biol* **2003**, *48*, 45–62.

3. Guo, M.; Chee, G.; O'Connell, D.; Dhou, S.; Fu, J.; Singhrao, K.; Ionascu, D.; Ruan, D.; Lee, P.; Low, D.A.; et al. Reconstruction of a high-quality volumetric image and a respiratory motion model from patient CBCT projections. *Med. Phys.* **2019**, *46*, 3627–3639, doi:10.1002/mp.13595.
4. Fassi, A.; Tagliabue, E.; Tirindelli, M.; Sarrut, D.; Riboldi, M.; Baroni, G. PO-0884: Respiratory motion models from Cone-Beam CT for lung tumour tracking. *Radiother. Oncol.* **2016**, doi:10.1016/s0167-8140(16)32134-x.
5. Fassi, A.; Bombardieri, A.; Ivaldi, G.B.; Liotta, M.; Tabarelli de Fatis, P.; Meaglia, I.; Porcu, P.; Riboldi, M.; Baroni, G. EP-1629: Lung tumor tracking using CBCT-based respiratory motion models driven by external surrogates. *Radiother. Oncol.* **2017**, doi:10.1016/s0167-8140(17)32064-9.
6. Zhang, Q.; Hu, Y.C.; Liu, F.; Goodman, K.; Rosenzweig, K.E.; Mageras, G.S. Correction of motion artifacts in cone-beam CT using a patient-specific respiratory motion model. *Med Phys* **2010**, *37*, 2901–2909.
7. Fassi, A.; Schaerer, J.; Fernandes, M.; Riboldi, M.; Sarrut, D.; Baroni, G. Tumor tracking method based on a deformable 4D CT breathing motion model driven by an external surface surrogate. *Int J Radiat Oncol Biol Phys* **2014**, *88*, 182–188, doi:S0360-3016(13)03113-1 [pii]10.1016/j.ijrobp.2013.09.026.
8. Li, R.; Lewis, J.H.; Jia, X.; Zhao, T.; Liu, W.; Wuenschel, S.; Lamb, J.; Yang, D.; Low, D. a; Jiang, S.B. On a PCA-based lung motion model. *Phys. Med. Biol.* **2011**, *56*, 6009–6030, doi:10.1088/0031-9155/56/18/015.
9. Dhou, S.; Hurwitz, M.; Mishra, P.; Berbeco, R.; Lewis, J. 4DCBCT-based motion modeling and 3D fluoroscopic image generation for lung cancer radiotherapy. In Proceedings of the Medical Imaging 2015: Image-Guided Procedures, Robotic Interventions, and Modeling; 2015.
10. Dhou, S.; Hurwitz, M.; Mishra, P.; Cai, W.; Rottmann, J.; Li, R.; Williams, C.; Wagar, M.; Berbeco, R.; Ionascu, D.; et al. 3D fluoroscopic image estimation using patient-specific 4DCBCT-based motion models. *Phys. Med. Biol.* **2015**, *60*, 3807–3824, doi:10.1088/0031-9155/60/9/3807.
11. Hurwitz, M.; Williams, C.L.; Mishra, P.; Rottmann, J.; Dhou, S.; Wagar, M.; Mannarino, E.G.; Mak, R.H.; Lewis, J.H. Generation of fluoroscopic 3D images with a respiratory motion model based on an external surrogate signal. *Phys. Med. Biol.* **2015**, *60*, 521–535, doi:10.1088/0031-9155/60/2/521.
12. Li, R.; Jia, X.; Lewis, J.H.; Gu, X.; Folkerts, M.; Men, C.; Jiang, S.B. Real-time volumetric image reconstruction and 3D tumor localization based on a single x-ray projection image for lung cancer radiotherapy. *Med Phys* **2010**, *37*, 2822–2826.
13. Lewis, J.; Li, R.; St. James, S.; Yue, Y.; Berbeco, R.; Mishra, P. Fluoroscopic 3D Images Based on 2D Treatment Images Using a Realistic Modified XCAT Phantom. *Int. J. Radiat. Oncol.* **2012**, doi:10.1016/j.ijrobp.2012.07.1972.
14. Mishra, P.; Li, R.; James, S.S.; Mak, R.H.; Williams, C.L.; Yue, Y.; Berbeco, R.I.; Lewis, J.H. Evaluation of 3D fluoroscopic image generation from a single planar treatment image on patient data with a modified XCAT phantom. *Phys Med Biol* **2013**, *58*, 841–858, doi:10.1088/0031-9155/58/4/841.
15. Zhang, Y.; Yin, F.F.; Segars, W.P.; Ren, L. A technique for estimating 4D-CBCT using prior knowledge and Limited-angle projections. *Med. Phys.* **2013**, doi:10.1118/1.4825097.
16. Li, R.; Lewis, J.H.; Jia, X.; Gu, X.; Folkerts, M.; Men, C.; Song, W.Y.; Jiang, S.B. 3D tumor localization through real-time volumetric x-ray imaging for lung cancer radiotherapy. *Med Phys* **2011**, *38*, 2783–2794.
17. Zhang, Q.; Pevsner, A.; Hertanto, A.; Hu, Y.-C.; Rosenzweig, K.E.; Ling, C.C.; Mageras, G.S. A patient-specific respiratory model of anatomical motion for radiation treatment planning. *Med. Phys.* **2007**, *34*, 4772–4781, doi:10.1118/1.2804576.
18. Berbeco, R.I.; Mostafavi, H.; Sharp, G.C.; Jiang, S.B. Towards fluoroscopic respiratory gating for lung tumours without radiopaque markers. *Phys Med Biol* **2005**, *50*, 4481–4490, doi:S0031-9155(05)87952-7 [pii]10.1088/0031-9155/50/19/004.
19. Sonke, J.J.; Zijp, L.; Remeijer, P.; van Herk, M. Respiratory correlated cone beam CT. *Med Phys* **2005**, *32*, 1176–1186.
20. Dhou, S.; Motai, Y.; Hugo, G.D. Local intensity feature tracking and motion modeling for respiratory signal extraction in cone beam CT projections. *IEEE Trans. Biomed. Eng.* **2013**, *60*, 332–342, doi:10.1109/TBME.2012.2226883.

21. Vergalasova, I.; Cai, J.; Yin, F.F. A novel technique for markerless, self-sorted 4D-CBCT: feasibility study. *Med Phys* **2012**, *39*, 1442–1451, doi:10.1118/1.3685443.
22. Park, S.; Kim, S.; Yi, B.; Hugo, G.; Gach, H.M.; Motai, Y. A Novel Method of Cone Beam CT Projection Binning Based on Image Registration. *IEEE Trans. Med. Imaging* **2017**, doi:10.1109/TMI.2017.2690260.
23. Chao, M.; Wei, J.; Li, T.; Yuan, Y.; Rosenzweig, K.E.; Lo, Y.C. Robust breathing signal extraction from cone beam CT projections based on adaptive and global optimization techniques. *Phys. Med. Biol.* **2016**, doi:10.1088/0031-9155/61/8/3109.
24. Yan, H.; Wang, X.; Yin, W.; Pan, T.; Ahmad, M.; Mou, X.; Cervino, L.; Jia, X.; Jiang, S.B. Extracting respiratory signals from thoracic cone beam CT projections. *Phys Med Biol* **2013**, *58*, 1447–1464, doi:10.1088/0031-9155/58/5/1447.
25. Kavanagh, A.; Evans, P.M.; Hansen, V.N.; Webb, S. Obtaining breathing patterns from any sequential thoracic x-ray image set. *Phys Med Biol* **2009**, *54*, 4879–4888, doi:S0031-9155(09)09758-9 [pii]10.1088/0031-9155/54/16/003.
26. Sabah, S.; Dhou, S. Image-based extraction of breathing signal from cone-beam CT projections. In Proceedings of the Proceedings of SPIE - The International Society for Optical Engineering; 2020; Vol. 11315.
27. Dhou, S.; Docef, A.; Hugo, G. Image-based respiratory signal extraction using dimensionality reduction for phase sorting in Cone-Beam CT Projections. In Proceedings of the ACM International Conference Proceeding Series; 2017; pp. 79–84.
28. Dhou, S.; Ionascu, D.; Williams, C.; Lewis, J. Inter-fraction variations in motion modeling using patient 4D-cone beam CT images. In Proceedings of the 2018 Advances in Science and Engineering Technology International Conferences, ASET 2018; 2018; pp. 1–4.
29. Dhou, S.; Lewis, J.; Cai, W.; Ionascu, D.; Williams, C. Quantifying day-to-day variations in 4DCBCT-based PCA motion models. *Biomed. Phys. Eng. Express* **2020**, *6*, doi:10.1088/2057-1976/ab817e.
30. Segars, W.P.; Mahesh, M.; Beck, T.J.; Frey, E.C.; Tsui, B.M.W. Realistic CT simulation using the 4D XCAT phantom. *Med. Phys.* **2008**, *35*, 3800–3808, doi:10.1118/1.2955743.
31. Segars, W.P.; Sturgeon, G.; Mendonca, S.; Grimes, J.; Tsui, B.M. 4D XCAT phantom for multimodality imaging research. *Med Phys* **2010**, *37*, 4902–4915.
32. Myronakis, M.E.; Cai, W.; Dhou, S.; Cifter, F.; Hurwitz, M.; Segars, P.W.; Berbeco, R.I.; Lewis, J.H. A graphical user interface for XCAT phantom configuration, generation and processing. *Biomed. Phys. Eng. Express* **2017**, doi:10.1088/2057-1976/aa5767.
33. Zijp, L.; Sonke, J.-J.; van Herk, M. Extraction of the respiratory signal from sequential thorax cone-beam X-ray images. In Proceedings of the International Conference on the Use of Computers in Radiation Therapy; 2004; pp. 507–509.
34. Van Herk, M.; Zijp, L.; Remeijer, P.; Wolthaus, J.; Sonke, J.J. On-line 4D cone beam CT for daily correction of lung tumour position during hypofractionated radiotherapy. *ICCR, Toronto, Canada* **2007**.
35. L. A. Feldkamp J. W. Kress, L.C.D. Practical cone-beam algorithm. *J. Opt. Soc. Am. A Opt. Image Sci. Vis.* **1984**, *1*, 612–619.
36. Rit, S.; Vila Oliva, M.; Brousmiche, S.; Labarbe, R.; Sarrut, D.; Sharp, G.C. The Reconstruction Toolkit (RTK), an open-source cone-beam CT reconstruction toolkit based on the Insight Toolkit (ITK). In Proceedings of the International Conference on the Use of Computers in Radiation Therapy (ICCR'13); 2013.
37. Lewis, J.H.; Li, R.; Watkins, W.T.; Lawson, J.D.; Segars, W.P.; Cervino, L.I.; Song, W.Y.; Jiang, S.B. Markerless lung tumor tracking and trajectory reconstruction using rotational cone-beam projections: a feasibility study. *Phys Med Biol* **2010**, *55*, 2505–2522, doi:S0031-9155(10)38937-8 [pii]10.1088/0031-9155/55/9/006.
38. Gu, X.; Pan, H.; Liang, Y.; Castillo, R.; Yang, D.; Choi, D.; Castillo, E.; Majumdar, A.; Guerrero, T.; Jiang, S.B. Implementation and evaluation of various demons deformable image registration algorithms on a GPU. *Phys Med Biol* **2010**, *55*, 207–219, doi:S0031-9155(10)30375-7 [pii]10.1088/0031-9155/55/1/012.
39. Cai, W.; Hurwitz, M.H.; Williams, C.L.; Dhou, S.; Berbeco, R.I.; Seco, J.; Mishra, P.; Lewis, J.H. 3D delivered dose assessment using a 4DCT-based motion model. *Med. Phys.* **2015**, *42*, 2897–2907, doi:10.1118/1.4921041.
40. Cai, W.; Dhou, S.; Cifter, F.; Myronakis, M.; Hurwitz, M.H.; Williams, C.L.; Berbeco, R.I.; Seco, J.; Lewis, J.H. 4D cone beam CT-based dose assessment for SBRT lung cancer treatment. *Phys. Med. Biol.* **2015**, doi:10.1088/0031-9155/61/2/554.

41. Chen, G.H.; Tang, J.; Leng, S. Prior image constrained compressed sensing (PICCS): a method to accurately reconstruct dynamic CT images from highly undersampled projection data sets. *Med Phys* **2008**, *35*, 660–663.
42. Sidky, E.Y.; Pan, X. Image reconstruction in circular cone-beam computed tomography by constrained, total-variation minimization. *Phys Med Biol* **2008**, *53*, 4777–4807, doi:10.1088/0031-9155/53/17/021.
43. Sidky, E.Y.; Duchin, Y.; Pan, X.; Ullberg, C. A constrained, total-variation minimization algorithm for low-intensity x-ray CT. *Med Phys* **2011**, *38 Suppl 1*, S117, doi:10.1118/1.3560887.
44. Choi, K.; Xing, L.; Koong, A.; Li, R. First study of on-treatment volumetric imaging during respiratory gated VMAT. *Med Phys* **2013**, *40*, 40701, doi:10.1118/1.4794925.
45. Choi, K.; Wang, J.; Zhu, L.; Suh, T.S.; Boyd, S.; Xing, L. Compressed sensing based cone-beam computed tomography reconstruction with a first-order method. *Med. Phys.* **2010**, doi:10.1118/1.3481510.
46. Li, T.; Koong, A.; Xing, L. Enhanced 4D cone-beam CT with inter-phase motion model. *Med Phys* **2007**, *34*, 3688–3695.
47. Rit, S.; Wolthaus, J.; van Herk, M.; Sonke, J.J. On-the-fly motion-compensated cone-beam CT using an a priori motion model. *Med Image Comput Comput Assist Interv* **2008**, *11*, 729–736.
48. Rit, S.; Sarrut, D.; Desbat, L. Comparison of analytic and algebraic methods for motion-compensated cone-beam CT reconstruction of the thorax. *IEEE Trans Med Imaging* **2009**, *28*, 1513–1525, doi:10.1109/TMI.2008.2008962.
49. Zhang, H.; Ma, J.; Bian, Z.; Zeng, D.; Feng, Q.; Chen, W. High quality 4D cone-beam CT reconstruction using motion-compensated total variation regularization. *Phys. Med. Biol.* **2017**, doi:10.1088/1361-6560/aa6128.
50. Li, T.; Schreibmann, E.; Yang, Y.; Xing, L. Motion correction for improved target localization with on-board cone-beam computed tomography. *Phys Med Biol* **2006**, *51*, 253–267, doi:10.1088/0031-9155/51/2/005.
51. Biguri, A.; Dosanjh, M.; Hancock, S.; Soleimani, M. A general method for motion compensation in x-ray computed tomography. *Phys. Med. Biol.* **2017**, doi:10.1088/1361-6560/aa7675.
52. Huang, X.; Zhang, Y.; Chen, L.; Wang, J. U-net-based deformation vector field estimation for motion-compensated 4D-CBCT reconstruction. *Med. Phys.* **2020**, doi:10.1002/mp.14150.
53. Riblett, M.J.; Christensen, G.E.; Weiss, E.; Hugo, G.D. Data-driven respiratory motion compensation for four-dimensional cone-beam computed tomography (4D-CBCT) using groupwise deformable registration. *Med. Phys.* **2018**, doi:10.1002/mp.13133.
54. Sauppe, S.; Kuhm, J.; Brehm, M.; Paysan, P.; Seghers, D.; Kachelrieß, M. Motion vector field phase-to-amplitude resampling for 4D motion-compensated cone-beam CT. *Phys. Med. Biol.* **2018**, doi:10.1088/1361-6560/aaa16d.
55. Weiss, G.H.; Talbert, A.J.; Brooks, R.A. The use of phantom views to reduce CT streaks due to insufficient angular sampling. *Phys Med Biol* **1982**, *27*, 1151–1162.
56. Lehmann, T.M.; Gonner, C.; Spitzer, K. Addendum: B-spline interpolation in medical image processing. *IEEE Trans Med Imaging* **2001**, *20*, 660–665, doi:10.1109/42.932749.
57. Bertram, M.; Wiegert, J.; Sch??fer, D.; Aach, T.; Rose, G. Directional view interpolation for compensation of sparse angular sampling in cone-beam CT. *IEEE Trans. Med. Imaging* **2009**, *28*, 1011–1022, doi:10.1109/TMI.2008.2011550.
58. Dhou, S.; Hugo, G.D.; Docef, A. Motion-based projection generation for 4D-CT reconstruction. In Proceedings of the 2014 IEEE International Conference on Image Processing, ICIP 2014; 2014.
59. Han, Y.; Ye, J.C. Framing U-Net via Deep Convolutional Framelets: Application to Sparse-View CT. *IEEE Trans. Med. Imaging* **2018**, doi:10.1109/TMI.2018.2823768.
60. Kelly, B.; Matthews, T.P.; Anastasio, M.A. Deep Learning-Guided Image Reconstruction from Incomplete Data. *arXiv* 2017.
61. Madesta, F.; Sentker, T.; Gauer, T.; Werner, R. Self-contained deep learning-based boosting of 4D cone-beam CT reconstruction. *Med. Phys.* **2020**, doi:10.1002/mp.14441.